

Nucleation and Precipitation Strengthening in Dilute Al-Ti and Al-Zr Alloys

KEITH E. KNIPLING, DAVID C. DUNAND, and DAVID N. SEIDMAN

Two conventionally solidified Al-0.2Ti alloys (with 0.18 and 0.22 at. pct Ti) exhibit no hardening after aging up to 3200 hours at 375 °C or 425 °C. This is due to the absence of Al₃Ti precipitation, as confirmed by electron microscopy and electrical conductivity measurements. By contrast, an Al-0.2Zr alloy (with 0.19 at. pct Zr) displays strong age hardening at both temperatures due to precipitation of Al₃Zr (L1₂) within Zr-enriched dendritic regions. This discrepancy between the two alloys is explained within the context of the equilibrium phase diagrams: (1) the disparity in solid and liquid solubilities of Ti in α -Al is much greater than that of Zr in α -Al; and (2) the relatively small liquid solubility of Ti in α -Al limits the amount of solute retained in solid solution during solidification, while the comparatively high solid solubility reduces the supersaturation effecting precipitation during post-solidification aging. The lattice parameter mismatch of Al₃Ti (L1₂) with α -Al is also larger than that of Al₃Zr (L1₂), further hindering nucleation of Al₃Ti. Classical nucleation theory indicates that the minimum solute supersaturation required to overcome the elastic strain energy of Al₃Ti nuclei cannot be obtained during conventional solidification of Al-Ti alloys (unlike for Al-Zr alloys), thus explaining the absence of Al₃Ti precipitation and the presence of Al₃Zr precipitation.

DOI: 10.1007/s11661-007-9283-6

© The Minerals, Metals & Materials Society and ASM International 2007

I. INTRODUCTION

THE Group 4 transition metals (Ti, Zr, or Hf) constitute a group of alloying additions to Al that show particular promise for developing creep-resistant, thermally stable Al-based alloys.^[1] In each of these systems, an ordered Al₃M (M = Ti, Zr, or Hf) trialuminide may be precipitated from a supersaturated solid solution during post-solidification aging. While the equilibrium structure of these Al₃M trialuminides is tetragonal (D0₂₂ or D0₂₃), decomposition of supersaturated Al-M solid solutions occurs initially by the formation of nanometer-scale metastable cubic Al₃M (L1₂) precipitates exhibiting small lattice parameter mismatches with α -Al, which transform to their respective equilibrium tetragonal structures after prolonged aging (approximately 100 to 1000 hours) at elevated temperatures (>450 °C). Moreover, these transition elements are anomalously slow diffusers in α -Al, with very limited equilibrium solid solubilities, enabling precipitated Al₃M to be resistant to Ostwald ripening

in accordance with volume diffusion-controlled coarsening models.^[1]

For high-temperature applications, Ti seems especially promising as an alloying addition among the Group 4 elements because it has the smallest atomic weight and the smallest diffusivity in α -Al.^[1] Indeed, Al alloys reinforced by Al₃Ti dispersions have garnered considerable interest as potential lightweight, high-temperature structural materials, and the thermal stability and strength at high temperatures of these alloys is well documented.^[2–18] These studies, however, investigated alloys prepared by rapid solidification processing (RSP)^[2–8] or mechanical alloying (MA)^[2,9–18] techniques, whose nonequilibrium processing routes circumvent the difficulties encountered during conventional solidification of Al-Ti alloys.

The problems with casting these alloys arise from the fact that Al₃M (M = Ti, Zr, or Hf) exhibits a peritectic phase equilibrium with the terminal α -Al solid solution. The first solid to form under equilibrium conditions is the properitectic, or primary, Al₃M ordered phase (for alloys in the peritectic composition range, *i.e.*, those enriched beyond the minimum liquid solubility of solute). These solute-rich primary phases readily nucleate and grow into coarse (approximately 100 μ m) precipitates during conventional casting, leaving the remaining melt, and ultimately the solidified α -Al solid solution, substantially depleted in solute. This limits the potential for subsequent precipitation strengthening because the supersaturation—and therefore the chemical driving force for solid-state nucleation, as well as the equilibrium volume fraction of the dispersed phase, if formed—is significantly reduced.

Under certain conditions, primary Al₃M may solidify from the melt with the metastable cubic L1₂ structure.^[19]

KEITH E. KNIPLING, formerly with the Department of Materials Science and Engineering, Northwestern University, Evanston, IL 60208-3108, National Research Council Associate, is with the Naval Research Laboratory, Washington, DC 20375-5320, USA. Contact e-mail: knipling@anvil.nrl.navy.mil DAVID C. DUNAND, James and Margie Krebs Professor of Materials Science and Engineering, is with the Department of Materials Science and Engineering, Northwestern University, Evanston, IL 60208-3108, USA. DAVID N. SEIDMAN, Walter P. Murphy Professor of Materials Science and Engineering, is with the Department of Materials Science and Engineering and Northwestern University, Evanston, IL 60208-3108, USA. Center for Atom-Probe Tomography (NUCAPT), Northwestern University.

Manuscript submitted December 15, 2006.

Article published online September 13, 2007.

These metastable particles are isostructural to, and exhibit a small lattice parameter mismatch with, the α -Al solid solution, and therefore act as efficient heterogeneous nucleants during solidification of α -Al. The resulting grain refinement in cast alloys is frequently exploited industrially by Ti additions to Al^[19–22] and has also been observed in Al-Zr^[19,23,24] and Al-Hf^[25–27] alloys when primary precipitation of Al₃M (L₂) occurs. The refined grain size, however, is undesirable for applications where creep resistance is required.

This study examines the feasibility of developing conventionally cast and aged, precipitation-strengthened, dilute Al-based alloys alloyed with the Group 4 elements Ti and Zr, exhibiting a coarse grain size suitable for creep-resistant applications. Most studies related to conventionally solidified Al-Ti alloys have focused on the thermal stability of the relatively coarse primary Al₃Ti phase formed during solidification.^[28–32] As noted in References 33 and 34, the scientific literature pertaining to decomposition or age hardening of Al-Ti solid solutions produced by conventional ingot metallurgy processing is rather limited. The primary objective, therefore, is to report and discuss the precipitation behavior in dilute Al-Ti alloys, with the data for Al-Zr provided primarily as a comparison. In a subsequent article,^[35] we report in detail on the precipitation behavior and stability of Al₃Zr in conventionally solidified Al-Zr alloys.

II. EXPERIMENTAL PROCEDURES

A. Alloy Compositions and Preparation

Two Al-Ti and one Al-Zr alloys were cast, with both solutes nominally alloyed at the 0.2 pct level (all compositions are given in at. pct); the exact alloy compositions are Al-0.18Ti, Al-0.22Ti, and Al-0.19Zr, with an estimated error of ± 0.01 at. pct, as indicated in Table I. Small (approximately 7 g) buttons of these alloys were prepared by arc melting in a gettered purified argon atmosphere using a nonconsumable tungsten electrode and a water-cooled copper cathode as the crucible. The charges were melted a minimum of 10 times and inverted between melts to ensure alloy homogeneity. The moderately enhanced cooling rate associated with the chilled crucible was estimated to be of the order of 10–100 °C s⁻¹. For dilute Al-Ti and Al-Zr alloys, as well as other peritectic systems, to a specific cooling rate corresponds a critical solute concentration below which primary precipitation of Al₃M (M = Ti or Zr) does not occur.^[36–38] The compositions

in Table I were expected, based on prior solidification studies (Figure 8, discussed subsequently), to be near the threshold for avoiding primary precipitation of Al₃M for the moderate cooling rates used here.

Both Al-Ti alloys were prepared by melting 99.95 at. pct Al (Atlantic Equipment Engineers, Bergenfield, NJ, and containing 257 at. ppm Fe and 260 at. ppm Si as impurities) with a monolithic Al₃Ti master alloy. A primary advantage of this approach is that the melting point of Al₃Ti (1350 °C) is lower than that of pure Ti (1688 °C). Additionally, this ordered structure is a line compound whose composition is entirely homogeneous. This is not true of commercial master alloys (containing typically 5 to 10 wt pct Ti) that exhibit coarse (approximately 100 μ m) primary Al₃Ti precipitates. For the dilute alloys in this investigation and the small mass of the button ingots, such inhomogeneous master alloys introduce unacceptable uncertainties in chemical composition. The monolithic Al₃Ti master alloy was prepared by arc melting the requisite amounts of pure constituents (99.95 pct Al, Atlantic Equipment Engineers; 99.99+ pct Ti, Alfa Aesar, Ward Hill, MA) corresponding to the stoichiometry of the Al₃Ti phase; chemical homogeneity and structural uniformity of the button ingot was verified using X-ray diffraction.

The Al-0.19Zr alloy was prepared from a dilute master alloy containing 1.9 wt pct Zr, which was dilution-cast from a commercial 10 wt pct Zr master alloy (KB Alloys, Reading, PA). The chemical compositions of both Al-Ti alloys were verified independently by Bodycote Materials Testing (Skokie, IL) and ATI Wah Chang (Albany, OR), while the composition of Al-0.19Zr was checked by ATI Wah Chang only.

B. Aging Treatments and Analytical Techniques

Prior to post-solidification aging, sections of each alloy were examined by optical microscopy and scanning electron microscopy (SEM) to verify the as-solidified microstructure (porosity and grain size) and to check for the presence of peritectic, or primary, Al₃M precipitates. The SEM micrographs of the as-solidified specimens were obtained with an Hitachi S-3500 instrument (Hitachi High Technologies America, Inc., Pleasanton, CA) operated at an accelerating voltage of 20 kV, using a secondary electron detector. The as-cast alloys were isothermally aged at 375 °C or 425 °C, within the range of temperatures reported to exhibit a strong age hardening response for Al-Ti alloys produced by RSP^[4,6,39,40] or MA^[10] and for Al-Zr alloys produced by RSP^[34,41–44] or chill casting.^[45,46] Precipitation of Al₃Ti or Al₃Zr during aging was monitored by a number of techniques, described subsequently.

First, Vickers microhardness measurements were performed at room temperature on metallographically polished sections using a load of 200 g and a dwell time of 5 seconds. Second, precipitation of Al₃Ti or Al₃Zr was assessed directly by transmission electron microscopy (TEM). The TEM foils were prepared by mechanical grinding sections of aged specimens to a thickness of approximately 100 μ m. Discs of 3-mm diameter were punched from these sections and thinned to perforation by

Table I. Designations and Verified Compositions of the Al-Ti and Al-Zr Alloys Investigated

Designation	First Analysis*	Second Analysis**
Al-0.18Ti	0.175 at. pct Ti	0.178 at. pct Ti
Al-0.22Ti	0.237 at. pct Ti	0.211 at. pct Ti
Al-0.19Zr	—	0.186 at. pct Zr

* Bodycote Materials Testing.

** ATI Wah Chang.

twin-jet electropolishing at 20 Vdc (Struers TenuPol-5*)

*TenuPol is a trademark of Struers A/S, Ballerup, Denmark.

using a 10 vol pct solution of perchloric acid in methanol at -40°C . Conventional TEM was performed on a Hitachi H-8100 operating at 200 kV or a PHILIPS** CM

**PHILIPS is a trademark of Philips Electronic Instruments Corp., Mahwah, NJ.

30 operating at 300 kV, using a double-tilt stage. Electropolished TEM foils were also examined using a LEO†

†LEO is a trademark of Zeiss-Leica, Cambridge, England.

1525 high-resolution field-emission gun scanning electron microscope (SEM) operated at 3 kV with a short working distance (3 mm) using a secondary electron in-lens detector. As discussed subsequently, the alloys are highly segregated on the micrometer scale, which is not easily discerned in TEM. The advantage of SEM as a complement to TEM is the much larger field-of-view from the larger range in magnification, which is compounded by the fact that there is no limitation that the foil be electron transparent. Furthermore, the resolution of the LEO 1525 is capable of resolving nanometer-scale Al_3Ti or Al_3Zr precipitates.

Finally, for the Al-Ti alloys, which did not exhibit detectable age hardening or evidence for precipitation of Al_3Ti by electron microscopy (SEM and TEM), electrical conductivity measurements were also performed to monitor the decomposition of the supersaturated solid solutions during extended aging at 425°C . These measurements were performed using a SIGMATEST 2.069 (Foerster Instruments, Pittsburgh, PA) eddy current apparatus at room temperature. Five measurements were recorded, each corresponding to a different frequency (60, 120, 240, 480, and 960 kHz), on each specimen. For consistency, a single specimen of each alloy (aged for various times) was used for conductivity measurements.

III. EXPERIMENTAL RESULTS

A. Optical Microscopy

Figure 1 shows the as-cast macrostructure of the alloys studied. The solidification macrostructure is typical of cast alloys, with coarse columnar grains, originating at the bottom surface of the ingot (which was in contact with the chilled copper crucible of the arc melter), growing upward toward a zone of equiaxed grains at the center of the ingot. The relative sizes of the columnar and equiaxed zones is strongly dependent on the solute content of the alloy and, more precisely, the extent of peritectic Al_3M ($\text{M} = \text{Ti}$ or Zr) precipita-

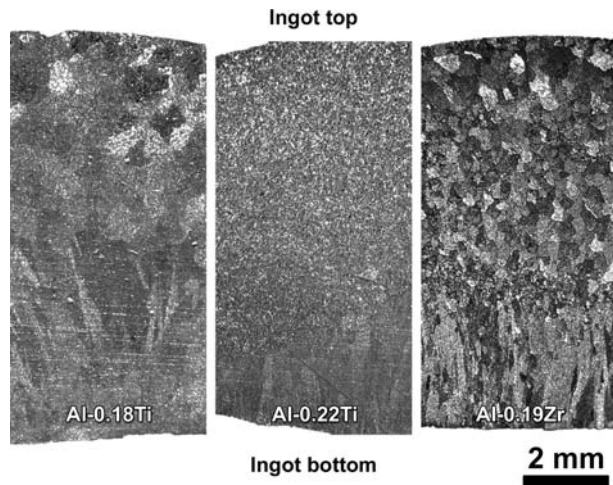
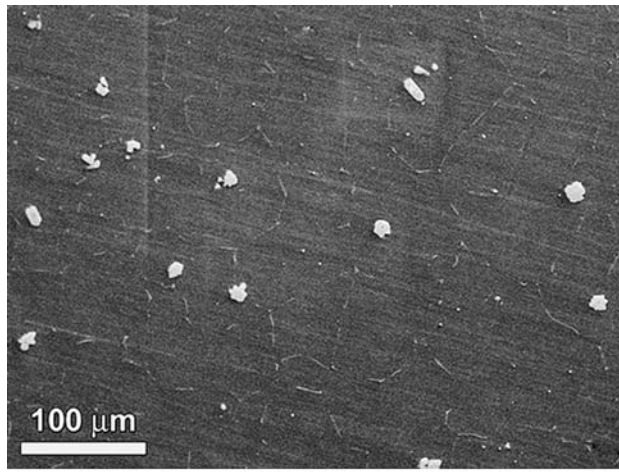


Fig. 1—Longitudinal cross sections of as-cast alloys Al-0.18Ti, Al-0.22Ti, and Al-0.19Zr, showing various degrees of grain refinement (etching with Poulton's reagent).

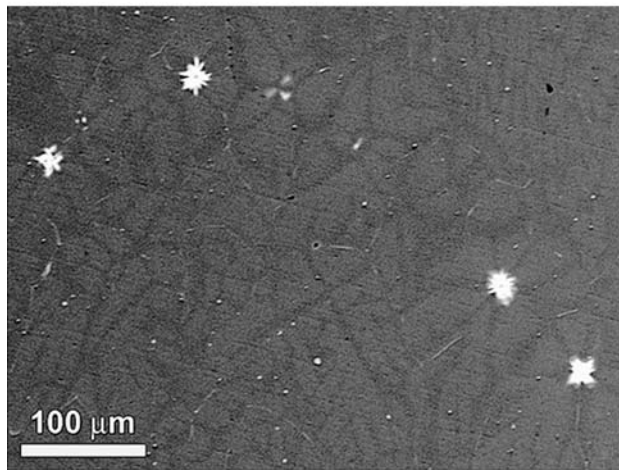
tion because these primary phases are potent grain refiners, as discussed previously.

Alloy Al-0.18Ti is the most dilute of those studied (Table I), and the extent of the columnar zone, which comprises nearly half of the ingot cross section in this alloy, is also greatest. Within the equiaxed zone, the grains are relatively coarse, with diameters ranging from 0.5 to 1.0 mm. The effect of a small increase in Ti concentration in these conventionally solidified alloys is demonstrated for Al-0.22Ti, which exhibits a dramatic refinement in grain size with a fine columnar zone that adjoins an even finer equiaxed region of small (50 to $100\ \mu\text{m}$) grains in the upper half of the ingot. Moderate grain refinement is also exhibited for Al-0.19Zr, which is intermediate between that of alloy Al-0.18Ti and alloy Al-0.22Ti. The columnar zone of Al-0.19Zr extends for approximately one-third of the ingot cross section, with the bulk of the ingot consisting of equiaxed grains ranging in size from 0.15 to 0.30 mm in diameter.

The pronounced grain refinement observed in Figure 1 for Al-0.22Ti and Al-0.19Zr is due to copious precipitation of peritectic Al_3Ti or Al_3Zr precipitates, which were observed in metallographically polished as-solidified specimens by SEM (Figure 2). The primary peritectic precipitates are 10 to $20\ \mu\text{m}$ in diameter and exhibit a petal-like morphology. This morphology is characteristic of the metastable L1_2 peritectic Al_3M phase,^[19] whose cubic structure is commensurate with fcc $\alpha\text{-Al}$ and acts as an effective heterogeneous nucleant of $\alpha\text{-Al}$ during solidification, resulting in the grain refinement observed in Figure 1. The refined grain structure is also apparent in Figure 2, as grain boundaries are apparent in both SEM micrographs. The grain boundaries are decorated with Fe-rich precipitates, confirmed by energy-dispersive X-ray spectroscopy in the SEM, and are thought to be a eutectic constituent formed at the end of solidification, as expected because the impurity Fe concentration is close to the maximum solubility of Fe in $\alpha\text{-Al}$.^[47]



(a)



(b)

Fig. 2—SEM secondary electron micrographs of as-solidified (a) Al-0.22Ti and (b) Al-0.19Zr. Both alloys exhibit petal-like primary Al_3Ti or Al_3Zr precipitates, responsible for the grain refinement observed in Fig. 1. Grain boundaries are visible in both micrographs, and Zr-enriched dendritic cells are apparent in (b).

The presence of the primary precipitates in Figure 2 indicates also that (for the conventional casting conditions used in this study) exceeding approximately 0.2 at. pct solute (Ti or Zr) results in primary precipitation of Al_3M and hence does not increase the amount of solute retained in solid solution. In addition to the primary precipitates described previously, Figure 2(b) reveals the Zr-enriched dendrites in as-solidified Al-0.19Zr, which appear lighter due to Z-contrast from backscattered electrons. A similar contrast is not as apparent in Al-0.22Ti (Figure 2(a)) because the difference in atomic number between Al (13) and Ti (22) is less than that of Zr (40). After aging, only the solute-enriched dendritic cells contain precipitates, as described subsequently.

B. Age Hardening

Figure 3 displays the evolution of microhardness of the Al-Ti and Al-Zr alloys upon isothermal aging at 375 °C or 425 °C. Each data point represents a minimum of 20 measurements, with the standard deviation of these measurements indicated by the error bars. At both temperatures, the Al-Ti alloys exhibit a negligible age hardening response after extended aging times up to 3,200 hours (19 weeks). This lack of strengthening contrasts with the significant precipitation hardening response of the Al-Zr alloy, which commences at times as short as 0.1 hours (6 minutes) at 425 °C and achieves peak strength within 25 hours at both 375 °C and 425 °C. As described subsequently, the pronounced strengthening is due to precipitation of small (< 10 nm) coherent Al_3Zr (L_{12}) precipitates; no evidence for precipitation of a similar Al_3Ti phase is observed. The as-cast hardness values of Al-0.22Ti and Al-0.19Zr are both 242 MPa, approximately 20 MPa greater than that of Al-0.18Ti. This moderate strength increase is probably attributable to solid solution strengthening from dissolved Ti or Zr in the as-cast alloys.^[48,49] While there is a refinement in the as-cast grain size with increasing solute concentration (Figure 1), Hall-Petch strengthening is not applicable because the scale of the microhardness

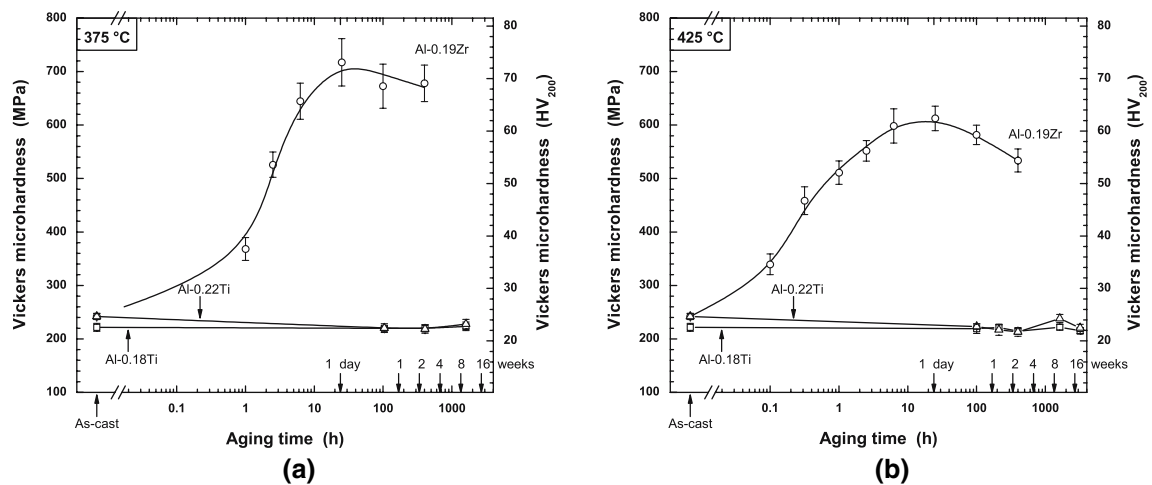


Fig. 3—Plot of Vickers microhardness vs aging time at (a) 375 °C and (b) 425 °C, for Al-0.18Ti, Al-0.22Ti, and Al-0.19Zr.

indent (approximately 125 μm across) is small as compared with the grain size.

C. Electron Microscopy

The origin of the precipitation-hardening response indicated in Figure 3 was investigated directly for Al-0.22Ti and Al-0.19Zr using SEM (Figure 4). The dendritic distribution of solute species formed during solidification in both alloys is revealed by preferential etching of the foil's surface during electropolishing. Figure 4(a) shows the as-cast structure for Al-0.22Ti, where the relief contrast around the dendrite arms is due to variations in solute concentration in solid solution between the dendritic and interdendritic regions of the alloy. The centers of the dendrites are enriched in solute^[36,50-52] and are apparently more resistant to electropolishing. Ryum^[53] observed similar resistance

to electropolishing in the dendritic cells of as-cast specimens of Al-Hf alloys. Figure 4(b) shows the same Al-0.22Ti alloy after aging for 1600 hours at 425 °C. The dendritic cells are delineated as previously, but no evidence for precipitation of Al_3Ti within the supersaturated cells is observed, consistent also with the negligible age hardening of the Al-Ti alloys demonstrated in Figure 3. Examination of the same specimen by TEM, both in real space (strain contrast) and reciprocal space (selected area electron diffraction), also provided no evidence for Al_3Ti precipitates or any other precipitated phase.

Figures 4(c) and 4(d) show SEM micrographs for Al-0.19Zr aged 400 hours at 425 °C. As with the Ti-containing alloys, dendrites are clearly delineated from the electropolishing process. Unlike the Al-Ti alloys, however, the solute-rich dendrites decompose during aging to form regions with a high number density of

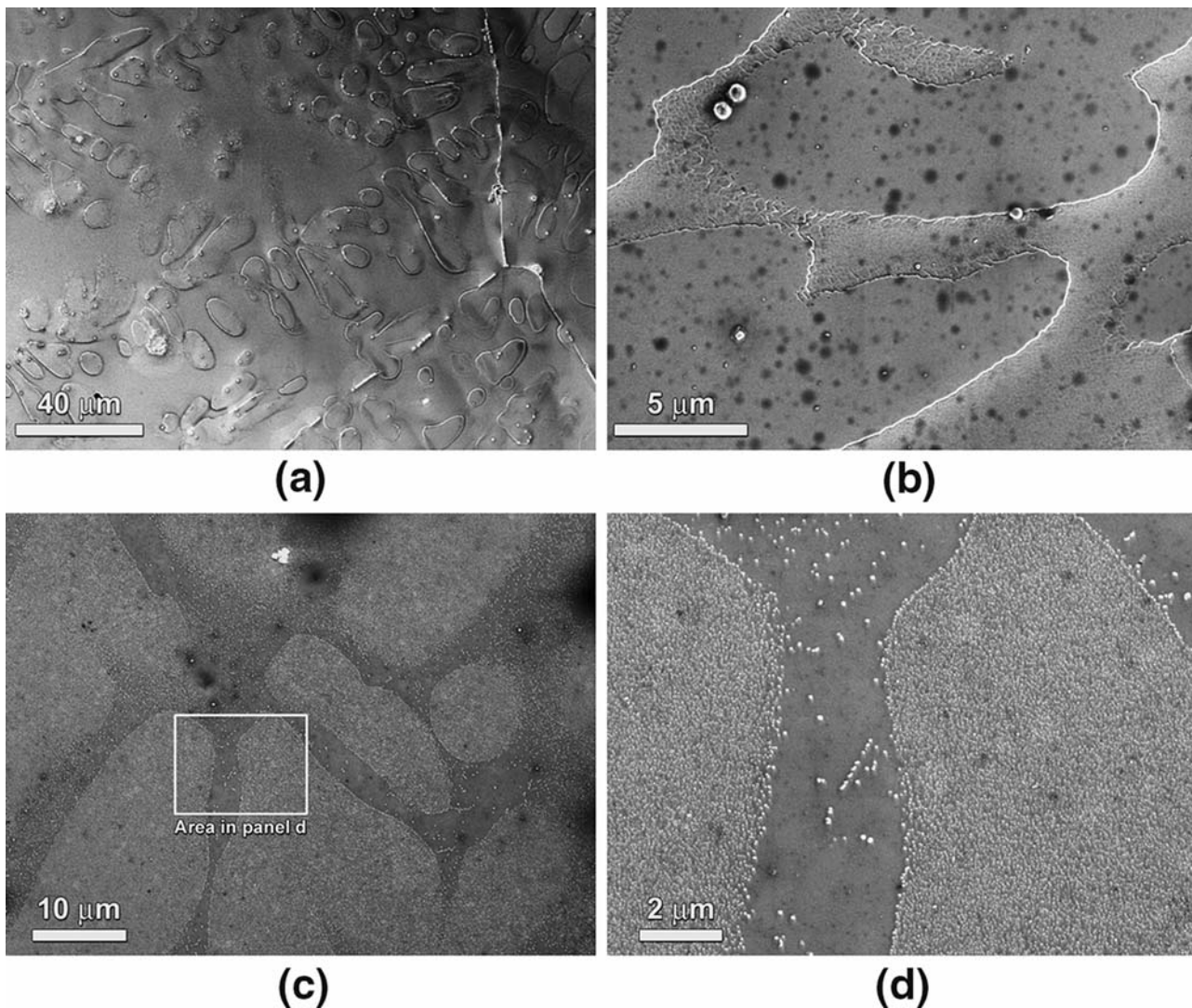


Fig. 4—SEM micrographs of electropolished TEM foils. (a) As-cast Al-0.22Ti, showing preferential etching around the solute-enriched dendrites. (b) Al-0.22Ti aged at 425 °C for 1600 h, showing no evidence of precipitation of Al_3Ti within the solute-enriched dendrites (black spots are pits from electropolishing). (c) Al-0.19Zr aged at 425 °C for 400 h, showing dendritic distributions of solute similar to panel (a). (d) Magnified view of panel (c), showing Al_3Zr dendritic regions with a high number density of small precipitates and interdendritic channels with isolated heterogeneously-nucleated precipitates of larger size.

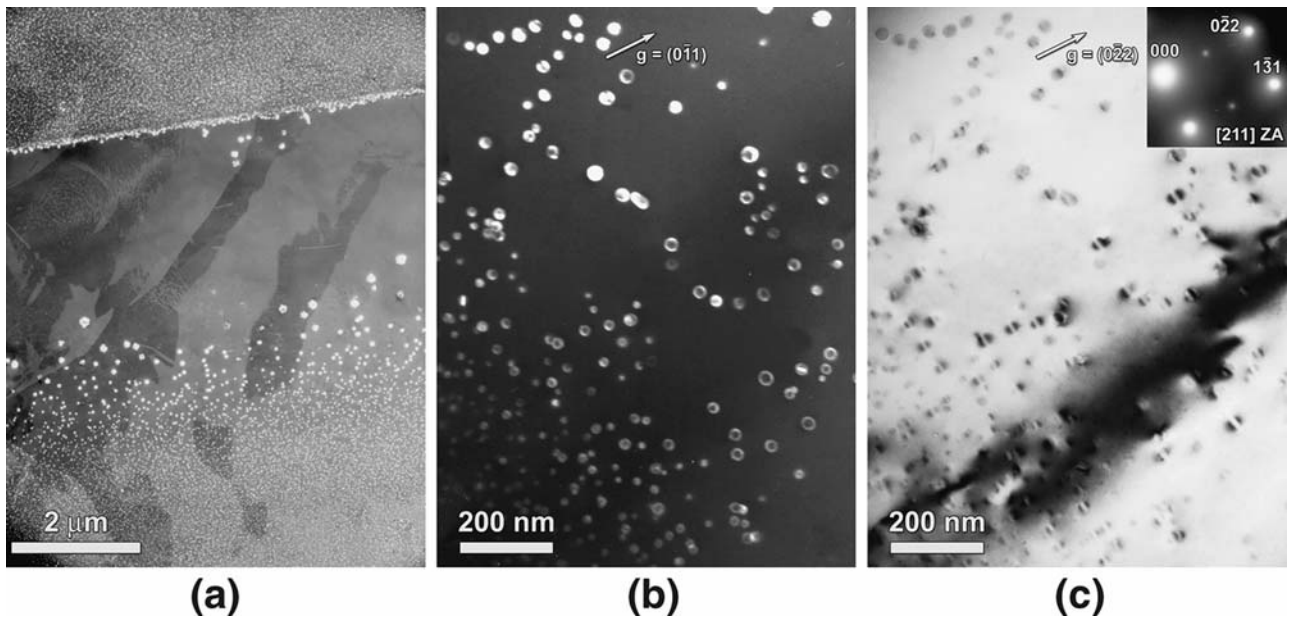


Fig. 5—TEM micrographs of Al-0.19Zr aged at 425 °C for 400 h. (a) Precipitate-rich dendritic regions separated by a precipitate-free interdendritic channel similar to those in Figs. 4(c) and 4(d). (b) Magnified view of Al₃Zr (L₁₂) precipitates near the dendrite periphery. (c) Complementary bright-field image of the region in (b). The strain fields surrounding the precipitates exhibit distinct lines of no-contrast normal to the diffraction vector, *g*, indicating that the precipitates are coherent with the α -Al solid solution.

homogeneously distributed, nanometer-scale Al₃Zr precipitates. Figure 5 shows superlattice dark-field TEM micrographs of the same Al-0.19Zr specimen, exhibiting again precipitate-rich and precipitate-free regions associated with the initial dendritic Zr distribution (Figure 5(a)). Within the center of the dendrites, where the solute supersaturation is largest, the small ($\langle R \rangle = 6.7 \pm 1.7$ nm) Al₃Zr precipitates have the metastable cubic L₁₂ structure and are homogeneously distributed in high number densities. The supersaturation decays with lateral position from the dendrite centers and, correspondingly, the precipitates become progressively larger and occur in smaller number densities (Figures 5(a) and (b)). Figure 5(c) is a complementary bright-field micrograph to that of Figure 5(b), recorded under two-beam conditions. The characteristic Ashby–Brown^[54] strain contrast surrounding the Al₃Zr (L₁₂) precipitates indicates that they are coherent with α -Al. It is the small, coherent, high number density Al₃Zr (L₁₂) precipitates within the dendrites that are responsible for the marked precipitation-hardening response of Al-0.19Zr presented in Figure 3.

D. Electrical Conductivity

The electrical conductivity of a disordered binary substitutional alloy is a parabolic function of the absolute solute concentration^[55] and is therefore a sensitive means of monitoring the decomposition of a supersaturated solid solution during aging. Electrical conductivity measurements were performed on both Al-Ti alloys (Al-0.18Ti and Al-0.22Ti) for extended aging times up to 1600 hours at 425 °C. No detectable change in conductivity was observed, indicating that

solute atoms remained dissolved in supersaturated solid solution and did not precipitate as Al₃Ti, corroborating the lack of precipitation observed by hardness and electron microscopy.

There was insufficient material to perform electrical conductivity measurements for the present Al-0.19Zr alloy. In a subsequent article,^[35] however, we monitor the decomposition of more-dilute Al-0.1 at. pct Zr alloys during isochronal aging, during which a significant increase in electrical conductivity is observed to accompany precipitation of Al₃Zr. Moreover, Royset and Ryum^[56] recently monitored in detail the decomposition kinetics of dilute Al-0.12 at. pct Sc alloys using a similar eddy current apparatus, indicating that the technique is sensitive enough to detect precipitation of Al₃M in dilute alloys.

IV. DISCUSSION

The hardness data in Figure 3 demonstrate that the Al-0.19Zr alloy exhibits pronounced precipitation hardening at 375 °C and 425 °C, unlike the Al-Ti alloys with similar solute concentrations. The strong age hardening response of the Zr-containing alloy is due to the precipitation of small (<10 nm) coherent Al₃Zr (L₁₂) precipitates, shown by SEM (Figures 4(c) and 4(d)) and TEM (Figure 5). No evidence for precipitation of a similar Al₃Ti phase is observed in the Al-Ti alloys by SEM or TEM. Moreover, there is no appreciable change in electrical conductivity after aging Al-0.18Ti or Al-0.22Ti at 425 °C for 1600 hours, which indicates that the Ti concentration in α -Al solid solution is unchanged, confirming the lack of precipitation of Al₃Ti.

A. Diffusion Kinetics

The measured tracer diffusivity of Ti in α -Al is smaller than that of Zr in α -Al at the aging temperatures employed, and it is conceivable that sluggish diffusion might account for the lack of Al_3Ti precipitation. The diffusivities, D , of Ti or Zr in α -Al are given by an Arrhenius relationship:

$$D = D_0 \cdot \exp\left(-\frac{Q}{R_g T}\right) \quad [1]$$

where R_g is the ideal gas constant, T is the absolute temperature, Q is the activation enthalpy for solute diffusion, and D_0 is the pre-exponential factor. With values $Q = 260$ and 242 kJ mol^{-1} and $D_0 = 1.12 \times 10^{-1}$ and $7.28 \times 10^{-2} \text{ m}^2 \text{ s}^{-1}$ for Ti and Zr, respectively,^[1] the diffusivity of Ti at $425 \text{ }^\circ\text{C}$ ($3.90 \times 10^{-21} \text{ m}^2 \text{ s}^{-1}$) is comparable to that of Zr at $375 \text{ }^\circ\text{C}$ ($2.26 \times 10^{-21} \text{ m}^2 \text{ s}^{-1}$). The hardness curve in Figure 3(a) demonstrates that the Al-Zr binary alloy reaches near-peak hardness by 6.25 hours of aging at $375 \text{ }^\circ\text{C}$, which corresponds to a root-mean-squared (RMS) diffusion distance, $\sqrt{4Dt}$ (where t is the aging time), of 14 nm for Zr atoms. For the slower-diffusing Ti atoms, a similar RMS diffusion distance can be achieved after 115 hours at $375 \text{ }^\circ\text{C}$ or 4 hours at $425 \text{ }^\circ\text{C}$, indicating that Ti atoms diffuse fast enough to support the nucleation and growth of Al_3Ti precipitates. Atom-probe tomography studies on Al-Sc-Ti alloys aged at $300 \text{ }^\circ\text{C}$ ^[57] and Al-Zr-Ti alloys aged at $375 \text{ }^\circ\text{C}$ or $425 \text{ }^\circ\text{C}$ ^[58] demonstrate that Ti segregates to the $\text{Al}_3(\text{Sc}_{1-x}\text{Ti}_x)$ and $\text{Al}_3(\text{Zr}_{1-x}\text{Ti}_x)$ precipitates, further evidence that the limited mobility of Ti is not the limiting factor explaining the lack of Al_3Ti precipitation.

B. Classical Nucleation Theory

The inability to nucleate Al_3Ti is a result of an insufficient supersaturation of Ti in solid solution following conventional solidification. Figures 6 and 7 display dilute equilibrium binary phase diagrams for the Al-Ti and Al-Zr systems based on experimental data. From a casting standpoint, a suitable alloying element with Al should produce a low liquidus temperature or, equivalently, exhibit high solubility in the liquid. This liquidus criterion minimizes, for a given alloy composition, the temperature required to form a single-phase melt and also reduces the tendency for primary phase precipitation during solidification.^[1] For precipitation strengthening, limited solid solubility is required to maximize the chemical driving force for nucleation as well as the volume fraction of the precipitated phase. As shown in Figures 6 and 7, the disparity in the liquid and solid solubilities of Ti in α -Al is much greater than that of Zr.

The equilibrium phase boundaries in Figures 6 and 7 correspond to the tetragonal-structured trialuminides: $\text{D}0_{22}$ for Al_3Ti ^[59] and $\text{D}0_{23}$ for Al_3Zr .^[60] The solubility limits of Ti and Zr in α -Al, in equilibrium with their respective metastable $\text{L}1_2$ structure Al_3M trialuminides, have been evaluated employing *ab initio* calculations by Liu *et al.*,^[61,62] who show that the ratio of the solid solubilities of the stable and metastable phases may be written as

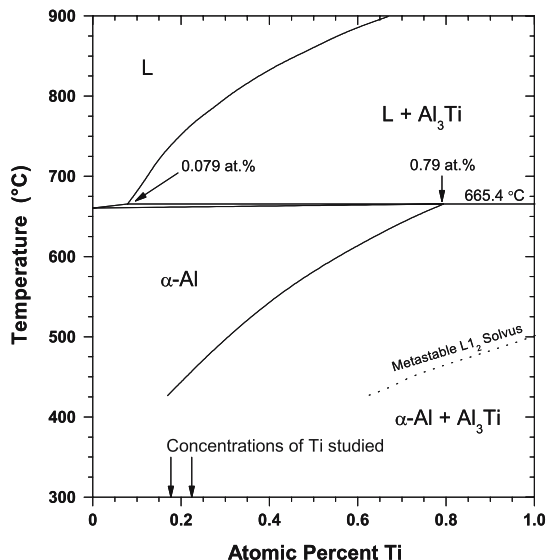


Fig. 6—Equilibrium Al-rich Al-Ti binary phase diagram (adapted from Murray^[59]) with metastable Al_3Ti ($\text{L}1_2$) solvus calculated by Liu *et al.*^[61,62]

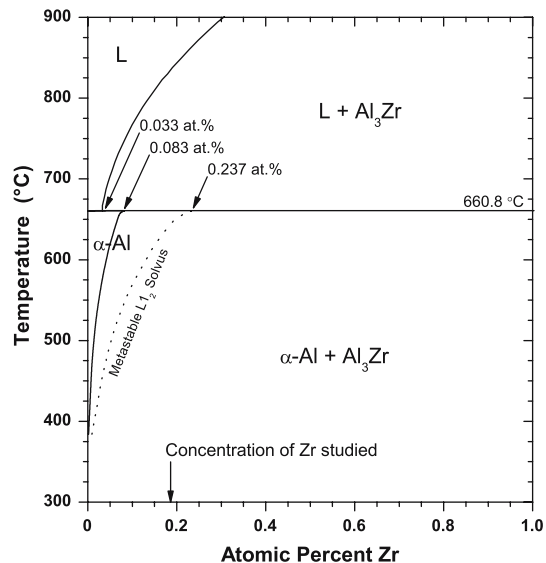


Fig. 7—Equilibrium Al-rich Al-Zr binary phase diagram (adapted from Murray^[60]) with metastable Al_3Zr ($\text{L}1_2$) solvus calculated by Liu *et al.*^[61,62]

$$\begin{aligned} C_{\text{ratio}}^{\text{Al}_3\text{Ti}} &= 0.816 \cdot \exp(1068/T) \\ C_{\text{ratio}}^{\text{Al}_3\text{Zr}} &= 0.710 \cdot \exp(1300/T) \end{aligned} \quad [2]$$

where $C_{\text{ratio}}^{\text{Al}_3\text{Ti}}$ and $C_{\text{ratio}}^{\text{Al}_3\text{Zr}}$ are the ratios of the solid solubility of Al_3Ti ($\text{L}1_2$) and Al_3Zr ($\text{L}1_2$) with their respective equilibrium ($\text{D}0_{22}$ or $\text{D}0_{23}$) solvus curves, and T is the absolute temperature. Using the equilibrium phase boundaries in Figures 6 and 7 as an accurate reference state, metastable $\text{L}1_2$ solvus boundaries are calculated using Eqs. [2] and are indicated by the dotted lines in Figures 6 and 7.

According to classical nucleation theory,^[63–67] the steady-state nucleation current (nucleation rate per unit volume) is given by

$$J \propto \exp\left(-\frac{\Delta F^*}{R_g T}\right) \exp\left(-\frac{Q}{R_g T}\right) \quad [3]$$

where ΔF^* is the net reversible work required for the formation of a critical nucleus, which is given by

$$\Delta F^* = \frac{16\pi\sigma^3}{3(\Delta F_{ch} - \Delta F_{el})^2} \quad [4]$$

The steady-state nucleation current, Eq. [3], is thus a function of the interfacial-free energy, σ ; the chemical driving force, ΔF_{ch} ; the reduction of ΔF_{ch} by the elastic strain energy, ΔF_{el} ; and the activation enthalpy for diffusion, Q , for diffusion of the solute. As discussed in Sections 1 through 4, the latter three parameters hinder the nucleation of Al_3Ti compared with Al_3Zr .

1. Chemical driving force, ΔF_{ch} , for nucleation of Al_3M

The metastable L_{12} solvus boundaries in Figures 6 and 7 demonstrate that the solid solubility of Ti in α -Al is significantly greater than that of Zr, which dictates the chemical driving force for homogenous nucleation of metastable L_{12} Al_3M ($\text{M} = \text{Ti}$ or Zr). Assuming ideal solution behavior (valid for the dilute concentrations discussed), this driving force is proportional to the natural logarithm of the supersaturation ratio, C_0/C_α , where C_0 is the concentration (atomic fraction) of M dissolved in solid solution and C_α is the solid solubility of M in α -Al given by Eq. [2]. Following Doherty,^[65] the chemical driving force per unit volume driving precipitation of the ordered Al_3M phase may be estimated as

$$\Delta F_{ch} = \frac{R_g T}{V_{\text{Al}_3\text{M}}} \left(\frac{C_{\text{Al}_3\text{M}} - C_\alpha}{1 - C_\alpha} \right) \ln \frac{C_0}{C_\alpha} \quad [5]$$

where $C_{\text{Al}_3\text{M}} = 0.25$ is the atomic fraction of solute in the ordered trialuminide, and $V_{\text{Al}_3\text{M}} = N_a (a_{\text{Al}_3\text{M}})^3 / 4$ is the molar volume of the precipitated phase (N_a is Avogadro's number and $a_{\text{Al}_3\text{M}} = 0.3967$ and 0.408 nm for Al_3Ti (L_{12}) and Al_3Zr (L_{12}), respectively^[11]).

Figures 6 and 7 indicate that, for a given solute concentration (C_0), the supersaturation driving precipitation of Al_3Zr is significantly greater than that for Al_3Ti , which partially explains the absence of precipitation of Al_3Ti because of the reduced supersaturation ratio C_0/C_α in Eq. [5]. The solute concentration C_0 , however, is not constant throughout the alloys because of the segregation visible in the SEM micrographs of Figure 4. For both Al-Ti and Al-Zr, the dendrites are supersaturated with respect to the overall bulk alloy composition, C_0 , and so in both cases the local supersaturation of solute in the dendrites is greater than the bulk compositions indicated in Table I and Figures 6 and 7.

The degree of this segregation was not measured directly (*e.g.*, by electron microprobe analysis (EPMA)) but may be estimated from the equilibrium solid-liquid partition coefficient, k_0 , that quantifies the difference in

the compositions of the solid and liquid phases in local equilibrium during solidification.^[68–70] Making the standard assumption that both the liquidus and solidus boundaries are straight lines, k_0 may be expressed as the ratio of the solid and liquid compositions at the peritectic temperature, $k_0 = C_S/C_L$. From Figures 6 and 7, $k_0 = 10$ for Ti, and $k_0 = 2.5$ for Zr; therefore, the first solid to form is predicted to be enriched by a factor of 10 and 2.5 for Ti and Zr, respectively. This is in reasonable agreement with the results of Bolling and colleagues,^[36,30] who measured, using EPMA, the concentration of Ti across the dendritic cells in Al-Ti alloys containing up to 0.28 at. pct Ti and observed a five- to sixfold enrichment in Ti at the dendrite centers. Setiukov and Fridlyander^[52] similarly observed that the Ti concentration in the central zones of the dendritic cells exceeded its average value by 6 to 8 times in alloys containing 0.02 to 0.17 at. pct Ti. All present Al-Ti and Al-Zr alloys are therefore locally supersaturated well beyond their respective equilibrium solubilities of solute, and so an insufficient supersaturation of solute, ΔF_{ch} , alone cannot account for the absence of Al_3Ti precipitates. As indicated in Eq. [4], the influence of elastic strain energy, ΔF_{el} , must also be considered because this reduces the net driving force for nucleation.

2. Reduction of the driving force by the elastic strain energy, ΔF_{el}

Solid-state reactions involve strain energy because precipitating a second phase, which is fully or partially coherent with the matrix, requires the straining of the lattices in both the matrix and precipitated phases. This elastic strain energy, ΔF_{el} , diminishes the net driving force, Eq. [4], and hence the rate of nucleation, Eq. [3]. Considering only dilatational strains and assuming elastic isotropy, the strain energy per unit volume for a coherent inclusion is given by^[64,67]

$$\Delta F_{el} = 2\mu \left(\frac{1+\nu}{1-\nu} \right) \delta^2 \quad [6]$$

where $\mu = 25.4$ GPa^[71] and $\nu = 0.345$ ^[72] are the shear modulus and Poisson's ratio of Al at room temperature. The average lattice parameter mismatches at room temperature, δ , of both the tetragonal ($\text{D}0_{22}$ or $\text{D}0_{23}$) and metastable cubic (L_{12}) phases are significantly greater for Al_3Ti ($\delta = 2.04$ pct and 5.36 pct for L_{12} and $\text{D}0_{22}$, respectively) than for Al_3Zr ($\delta = 0.75$ pct and 2.89 pct for L_{12} and $\text{D}0_{23}$, respectively).^[11] Thus, the elastic strain energy preventing nucleation of Al_3Ti (L_{12}) is more than 7 times greater than that of Al_3Zr (L_{12}). The lattice parameter mismatch δ , and thus the elastic strain energy is, however, expected to decrease somewhat at higher temperatures, owing to differences in thermal expansion between the α -Al matrix and the Al_3M precipitates.^[73,74] Similarly, the shear modulus at higher temperature is somewhat reduced.

3. Critical solute concentration, C_0 , to overcome ΔF_{el}

Compared with Al_3Zr (L_{12}), nucleation of Al_3Ti (L_{12}) is hindered by the following: (1) a reduced chemical driving force (ΔF_{ch}) for a given C_0 ; and (2) a greater

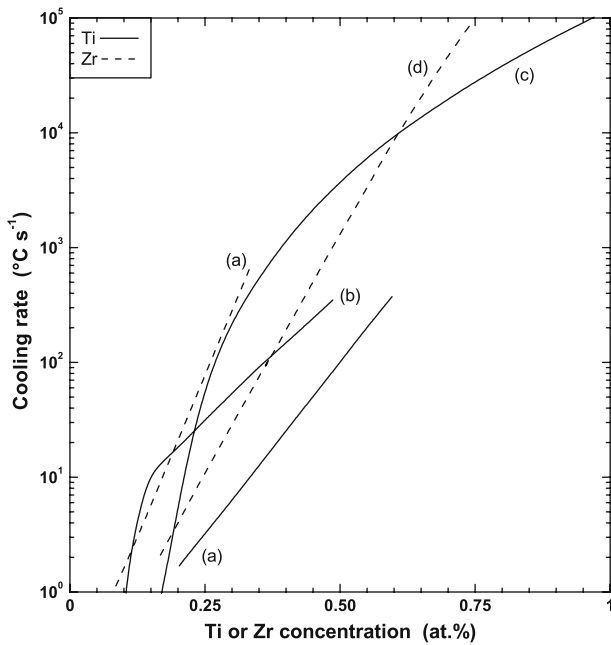


Fig. 8—Critical cooling rate for suppressing primary Al_3Ti (solid lines) or Al_3Zr (dashed lines) and achieving supersaturated $\alpha\text{-Al}$ solid solution, as reported by (a) Ohashi and Ichikawa,^[19] (b) Kerr *et al.*,^[36] (c) Hori *et al.*,^[75, 76] and (d) Hori *et al.*^[24]

elastic strain energy opposing nucleation (ΔF_{el}). To explain why nucleation of Al_3Zr (L_{12}) is observed and that of Al_3Ti (L_{12}) is not, consider the relative magnitudes of ΔF_{ch} and ΔF_{el} entering Eq. [4] for both systems. The chemical driving force, ΔF_{ch} (Eq. [5]), is calculated substituting $C_\alpha = 0.0063$ for Al_3Ti (L_{12}) and $C_\alpha = 0.0002$ for Al_3Zr (L_{12}), using Eq. [2] at 425 °C. Substituting the appropriate values for $V_{\text{Al}_3\text{M}}$, $\Delta F_{ch} = 151.4 \ln(158.7C_0)$ for Al_3Ti (L_{12}), and $\Delta F_{ch} = 141.9 \ln(5000C_0)$ for Al_3Zr (L_{12}). The elastic strain energy, ΔF_{el} (Eq. [6]), is 45 MJ mol⁻¹ and 6 MJ mol⁻¹ for Al_3Ti (L_{12}) and Al_3Zr (L_{12}), respectively. Equating ΔF_{ch} and ΔF_{el} gives a critical solute concentration necessary to overcome the elastic strain energy barrier associated with precipitate nucleation. For Al-Ti alloys, the critical value of C_0 is 0.84 at. pct Ti, and for Al-Zr, it is 0.021 at. pct Zr.

Table I indicates that the bulk compositions of both Al-Ti alloys studied are less than the critical threshold of 0.84 at. pct Ti, whereas Al-0.19Zr is supersaturated well beyond 0.021 at. pct Zr, thus explaining the observed precipitation of Al_3Zr (L_{12}) and the lack thereof for Al_3Ti . This explanation is not strictly complete because, as discussed, the alloys are segregated and hence locally supersaturated beyond the bulk compositions in Table I. Nevertheless, it is the combination of a small chemical driving force, ΔF_{ch} , coupled with a large elastic strain energy barrier, ΔF_{el} , in the Al-Ti system, as compared with the Al-Zr system, that explains their disparate precipitation behavior.

4. Activation enthalpy for solute diffusion, Q

Equation [3] indicates that the nucleation current is strongly dependent on temperature. The solute supersaturation (and, correspondingly, ΔF_{ch}) increases with

decreasing temperature (Eq. [2]), while the solute diffusivity D decreases exponentially (Eq. [1]). These competing influences result in an intermediate temperature for optimum nucleation kinetics.^[66] As discussed in Section IV-A, the activation enthalpy for solute diffusion, Q , for Ti in $\alpha\text{-Al}$ (260 kJ mol⁻¹) is greater than that of Zr (242 kJ mol⁻¹), which increases the temperature for maximum nucleation current for Al_3Ti . As discussed, the value of ΔF_{ch} driving precipitation of Al_3Ti is significantly less than that for Al_3Zr for a given C_0 (Figures 6 and 7). This reduced ΔF_{ch} is exacerbated by the higher Q for Ti diffusion because at the temperatures where Ti is mobile, the supersaturation is not large enough to effect nucleation of Al_3Ti .

C. Limitations on Increasing the Solute Concentration

The discussion in Section IV-B indicates that an increased concentration of Ti (C_0) beyond those we studied is required for precipitation of Al_3Ti . This, however, is not possible under conventional casting conditions. As demonstrated in Figure 1, the marked grain refinement observed with increasing Ti concentration is due to primary precipitation of Al_3Ti in the melt, and increasing the Ti concentration does not increase the amount of Ti retained in $\alpha\text{-Al}$ solid solution. The inter-relationships among solidification rates, solute concentrations, and solidified microstructures of the Al-Ti and Al-Zr binary systems have been the subject of prior studies,^[19,24,36,75,76] which are summarized in Figure 8. These curves show the measured solidification rate, as a function of solute concentration, necessary to suppress primary precipitation of Al_3Ti or Al_3Zr , thereby obtaining supersaturated $\alpha\text{-Al}$ solid solution. Figure 8 indicates that to achieve a concentration of 0.84 at. pct Ti supersaturated in a homogeneous $\alpha\text{-Al}$ solid solution, required to just offset the elastic strain energy associated with nucleation of Al_3Ti (L_{12}), cooling rates of nearly 5×10^4 °C s⁻¹ (based on the data of Hori *et al.*^[75,76]) are required. To achieve a greater driving force for nucleation, still higher cooling rates are required. Nucleation of Al_3Zr (L_{12}) requires a small supersaturation to overcome the elastic strain energy barrier, and the critical composition of 0.021 at. pct Zr is readily achieved for even the slowest cooling rates in Figure 8.

D. Comparison with Previous Studies

In contrast to the closely related Al-Zr and Al-Hf systems, the precipitation behavior of Al_3Ti in Al-Ti alloys has been debated in the scientific literature. As with Al-Zr and Al-Hf alloys, the decomposition sequence of supersaturated Al-Ti solid solutions has been reported to occur first by the precipitation of a metastable Al_3Ti (L_{12}) phase, which then transforms to the equilibrium tetragonal (D_{022}) structure after prolonged aging.^[1] Asboll and Ryum,^[77] however, observed only precipitation of the equilibrium D_{022} phase in chill-cast Al-0.34 at. pct Ti alloys aged between 400 °C and 550 °C. They also noted that the decomposition kinetics of Al_3Ti were sluggish compared with those of Al alloyed with other elements of the same subgroup, Zr or

Hf. Pandey and Suryanarayana^[78] also compared the decomposition behavior of rapidly solidified Al alloyed with Ti, Zr, or Hf (Group 4 elements) and noted that a metastable Al_3M (L_{12}) ordered phase is observed in Al-Zr and Al-Hf alloys but not in Al-Ti alloys. This result agrees with other studies^[8,32,43] reporting only precipitation of the equilibrium D_{022} phase in Al-Ti alloys aged in the broad temperature range of 200 °C to 600 °C.

Other studies report no precipitation during aging of supersaturated Al-Ti solid solutions. Ohashi *et al.*^[79] found no evidence for precipitation of Al_3Ti , using microhardness and electrical resistivity measurements, in Al-Ti alloys containing up to 0.45 at. pct Ti produced by RSP during 100 hours of aging in the range of 400 °C to 640 °C. St. John *et al.*^[31] also observed no solid-state precipitation of Al_3Ti when aging an Al-1.1 at. pct Ti alloy for 24 hours at 435 °C; their alloy did, however, contain coarse primary Al_3Ti precipitates, indicating that the amount of Ti initially in solid solution was reduced.

Nucleation of coherent Al_3Ti (L_{12}) precipitates has been reported only for highly supersaturated alloys produced by nonequilibrium means (RSP). Ohashi and Ichikawa^[51] observed Al_3Ti (L_{12}) precipitates in alloys containing 0.3 to 1.4 at. pct Ti aged at 400 °C to 500 °C. Muddle and co-workers^[4,39,80,81] observed precipitation of coherent Al_3Ti (L_{12}) in melt-spun alloys containing 2.9 to 3.5 at. pct Ti aged at 300 °C to 500 °C. Similar supersaturations cannot be achieved by conventional casting (Figures 1 and 8) because Ti precipitates in the liquid as peritectic Al_3Ti at moderate cooling rates.

E. Common Industrial Uses of Ti and Zr Additions to Al

Perhaps the most illustrative comparison of Al-Ti and Al-Zr alloys is found by considering their primary industrial roles. As discussed, minor additions of Ti are used to refine the grain structure in commercial aluminum alloys, where primary Al_3Ti precipitates act as heterogeneous nuclei during solidification of the melt.^[19–22] A solid-state counterpart to this grain refinement effect is realized when dilute additions of Zr are added to commercial wrought alloys as recrystallization inhibitors.^[82–85] Small (20 to 30 nm) coherent Al_3Zr (L_{12}) precipitates, formed during post-solidification aging, are effective barriers to grain-boundary migration. Titanium is thus added to form primary precipitates in the melt, whereas Zr is used to form coherent dispersoids precipitated from supersaturated solid solution. This suggests that (1) Zr, compared with Ti, is easier to retain in solid solution during conventional solidification; and (2) Al_3Zr , compared with Al_3Ti , is more readily precipitated during post-solidification aging. These considerations indicate that the Al-Zr system is a better candidate than the Al-Ti system for developing a castable, precipitation-strengthened alloy.

V. CONCLUSIONS

This investigation has compared the decomposition of supersaturated, conventionally cast Al-0.2 at. pct Ti and

Al-0.2 at. pct Zr alloys, upon aging at 375 °C or 425 °C. The Zr-containing alloy exhibits a strong age hardening response after about 24 hours at both temperatures, due to copious precipitation of coherent, nanometer-scale Al_3Zr (L_{12}) precipitates within the supersaturated dendritic cells of the alloy. Precipitation of a similar Al_3Ti phase in supersaturated dendrites is not observed, even for much longer aging times (up to 3200 hours at 425 °C). Compared with Al_3Zr , nucleation of Al_3Ti (L_{12}) is hindered by the following: (1) a reduced chemical driving force (ΔF_{ch}) for nucleation (for a given local alloy composition, C_0); (2) a larger elastic strain energy opposing nucleation (ΔF_{el}); and (3) a greater activation enthalpy for solute diffusion, Q .

Despite Ti enrichment in dendritic regions, the minimum supersaturation to produce solid-state Al_3Ti precipitation cannot be achieved in conventionally solidified binary Al-Ti alloys because increasing the Ti concentration beyond the levels we have studied causes crystallization of primary Al_3Ti during solidification and thus does not increase the solute available in solid solution for subsequent precipitation. By contrast, the Al-Zr system is more promising for developing a castable, precipitation-hardened alloy with good coarsening and creep resistance.

ACKNOWLEDGMENTS

This research was supported by the United States Department of Energy, Basic Sciences Division, under Contract No. DE-FG02-02ER45997. Gratitude is expressed to KB Alloys for providing the Al-Zr master alloy. We are indebted to Dr. J.L. Murray (Alcoa), for providing the most recent and reliable data for the binary Al-Ti and Al-Zr phase diagrams. We also thank Dr. J.Z. Liu and Professor M. Asta (Northwestern University and University of California, Davis), for calculating the metastable L_{12} solvus curves for Al_3Ti and Al_3Zr , and Professor M.E. Fine (Northwestern University) for useful discussions.

REFERENCES

1. K.E. Knippling, D.C. Dunand, and D.N. Seidman: *Z. Metallkd.*, 2006, vol. 97, pp. 246–65.
2. H. Jones and W.M. Rainforth: *Metall. Mater. Trans. A*, 2003, vol. 34A, pp. 419–21.
3. J.F. Nie, S. Sridhara, and B.C. Muddle: *Metall. Trans. A*, 1992, vol. 23A, pp. 3193–205.
4. J.F. Nie, A. Majumdar, and B.C. Muddle: *Mater. Sci. Eng. A*, 1994, vol. 179, pp. 619–24.
5. J.F. Nie and B.C. Muddle: *Mater. Sci. Eng. A*, 1996, vol. 215, pp. 92–103.
6. W.E. Frazier and M.J. Koczak: in *High Strength Powder Metallurgy Aluminum Alloys II*, G.J. Hildeman and M.J. Koczak, eds., TMS, Warrendale, PA, 1986, pp. 353–66.
7. J.M. Wu, S.L. Zheng, and Z.Z. Li: *Mater. Sci. Eng. A*, 2000, vol. 289, pp. 246–54.
8. Y. Wang, Z. Zhang, W. Wang, and X. Bian: *Mater. Sci. Eng. A*, 2004, vol. 366, pp. 17–24.
9. G.X. Liang, Z.C. Li, and E. Wang: *J. Mater. Sci.*, 1996, vol. 31, pp. 901–04.

10. W.E. Frazier and M.J. Koczak: *Scripta Metall.*, 1987, vol. 21, pp. 129–34.
11. G.S. Murty, M.J. Koczak, and W.E. Frazier: *Scripta Metall.*, 1987, vol. 21, pp. 141–46.
12. J.A. Hawk, P.K. Mirchandani, R.C. Benn, and H.G.F. Wilsdorf: in *Dispersion Strengthened Aluminum Alloys*, Y.W. Kim and W.M. Griffith, eds., TMS, Warrendale, PA, 1988, pp. 551–72.
13. J.A. Hawk, K.R. Lawless, and H.G.F. Wilsdorf: *Scripta Metall.*, 1989, vol. 23, pp. 119–24.
14. J.A. Hawk, J.K. Briggs, and H.G.F. Wilsdorf: in *Advances in Powder Metallurgy*, T.G. Gasbarre and W.F. Jandeska, eds., MPIF, Princeton, NJ, 1989, pp. 285–99.
15. P.K. Mirchandani, R.C. Benn, and K.A. Heck: in *Lightweight Alloys for Aerospace Applications*, E.W. Lee, E.H. Chia and N.J. Kim, eds., TMS, Warrendale, PA, 1989, pp. 33–58.
16. P.K. Mirchandani, D.O. Gothard, and A.I. Kemppinen: in *Advances in Powder Metallurgy*, T.G. Gasbarre and W.F. Jandeska, eds., MPIF, Princeton, NJ, 1989, pp. 161–73.
17. S.H. Wang and P.W. Kao: *Acta Mater.*, 1998, vol. 46, pp. 2675–82.
18. I.C. Barlow, H. Jones, and W.M. Rainforth: *Acta Mater.*, 2001, vol. 49, pp. 1209–24.
19. T. Ohashi and R. Ichikawa: *Z. Metallkd.*, 1973, vol. 64, pp. 517–21.
20. F.A. Crossley and L.F. Mondolfo: *Trans. AIME*, 1951, vol. 191, pp. 1143–48.
21. D.G. McCartney: *Int. Mater. Rev.*, 1989, vol. 34, pp. 247–60.
22. B.S. Murty, S.A. Kori, and M. Chakraborty: *Int. Mater. Rev.*, 2002, vol. 47, pp. 3–29.
23. W. Dahl, W. Gruhl, W.G. Burchard, G. Ibe, and C. Dumitrescu: *Z. Metallkd.*, 1977, vol. 68, pp. 121–27.
24. S. Hori, S. Saji, and A. Takehara: in *Proc. 4th Int. Conf. on Rapidly Quenched Metals*, T. Masumoto and K. Suzuki, eds., The Japan Institute of Metals, Sendai, Japan, 1981, pp. 1545–48.
25. S. Hori and N. Furushiro: in *Proc. 4th Int. Conf. on Rapidly Quenched Metals*, T. Masumoto and K. Suzuki, eds., The Japan Institute of Metals, Sendai, Japan, 1981, pp. 1525–28.
26. S. Hori, N. Furushiro, and W. Fujitani: *J. Jpn. Inst. Light Met.*, 1980, vol. 30, pp. 617–25.
27. A.F. Norman and P. Tsakiroopoulos: *Int. J. Rapid Solid.*, 1991, vol. 6, pp. 185–213.
28. W.L. Fink, K.R. van Horn, and P.M. Budge: *AIMME Trans.*, 1931, vol. 93, pp. 421–39.
29. H.A.F. El-Halfawy, E.S.K. Menon, M. Sundararaman, and P. Mukhopadhyay: *Metallography*, 1979, vol. 12, pp. 257–62.
30. H.A.F. El-Halfawy: in *Titanium '80—Science and Technology—4th Int. Conf. on Titanium*, H. Kimura and O. Izumi, eds., TMS, Warrendale, PA, 1980, pp. 1379–87.
31. D.H. St John and L.M. Hogan: *J. Mater. Sci.*, 1980, vol. 15, pp. 2369–75.
32. K. Venkateswarlu, S.K. Das, M. Chakraborty, and B.S. Murty: *Mater. Sci. Eng. A*, 2003, vol. 351, pp. 237–43.
33. N.F. Levoy and J.B. Vander Sande: *Metall. Trans. A*, 1989, vol. 20A, pp. 999–1019.
34. P. Malek, M. Janecek, and B. Smola: *Kov. Mater.*, 2000, vol. 38, pp. 160–77.
35. K.E. Knippling, D.C. Dunand, and D.N. Seidman: unpublished research, 2007.
36. H.W. Kerr, J. Cisse, and G.F. Bolling: *Acta Metall.*, 1974, vol. 22, pp. 677–86.
37. H.W. Kerr and W. Kurz: *Int. Mater. Rev.*, 1996, vol. 41, pp. 129–64.
38. D.H. St. John and L.M. Hogan: *J. Mater. Sci.*, 1982, vol. 17, pp. 2413–18.
39. J.F. Nie and B.C. Muddle: *Mater. Sci. Eng. A*, 1996, vol. 221, pp. 11–21.
40. B.S. You and W.W. Park: *Scripta Mater.*, 1996, vol. 34, pp. 201–05.
41. T. Ohashi and R. Ichikawa: *J. Jpn. Inst. Met.*, 1970, vol. 34, pp. 604–10.
42. V. Dobatkin, V.I. Elagin, V.M. Federov, and R.M. Sizova: *Russ. Metall.*, 1970, pp. 122–27.
43. W.W. Park and T.H. Kim: *J. Kor. Inst. Met.*, 1985, vol. 3, pp. 11–18.
44. W.W. Park and T.H. Kim: *Scripta Metall.*, 1988, vol. 22, pp. 1709–14.
45. R. Ichikawa and T. Ohashi: *J. Jpn. Inst. Light Met.*, 1968, vol. 18, pp. 314–19.
46. T. Sato, A. Kamio, and G.W. Lorimer: *Mater. Sci. Forum*, 1996, vols. 217–222, pp. 895–900.
47. H. Okamoto: *Phase Diagrams of Dilute Binary Alloys*, ASM INTERNATIONAL, Materials Park, OH, 2002.
48. E. Babic, E. Girt, R. Krsnik, B. Leontic, M. Ocko, Z. Vucic, and I. Zoric: *Physica Status Solidi A*, 1973, vol. 16, pp. K21–K25.
49. E. Sahin and H. Jones: in *Rapidly Quenched Metals II*, B. Cantor, ed., The Metals Society, London, 1978, pp. 138–46.
50. J. Cisse, H.W. Kerr, and G.F. Bolling: *Metall. Trans.*, 1974, vol. 5, pp. 633–41.
51. T. Ohashi and R. Ichikawa: *J. Jpn. Inst. Light Met.*, 1977, vol. 27, pp. 105–12.
52. O.A. Setiukov and I.N. Fridlyander: *Mater. Sci. Forum*, 1996, vols. 217–222, pp. 195–200.
53. N. Ryum: *J. Mater. Sci.*, 1975, vol. 10, pp. 2075–81.
54. M.F. Ashby and L.M. Brown: *Phil. Mag.*, 1963, vol. 8, pp. 1083–1102.
55. V.L. Nordheim: *Ann. Phys.*, 1931, vol. 9, pp. 641–78.
56. J. Royset and N. Ryum: *Mater. Sci. Eng. A*, 2005, vol. 396, pp. 409–22.
57. M.E. van Dalen, D.C. Dunand, and D.N. Seidman: *Acta Mater.*, 2005, vol. 53, pp. 4225–35.
58. K.E. Knippling, D.C. Dunand, and D.N. Seidman: *Microsc. Microanal.*, 2006, accepted for publication.
59. J.L. Murray: Alcoa, Alcoa Center, PA, personal communication, 2005.
60. J.L. Murray, A. Peruzzi, and J.P. Abriata: *J. Phase Equil.*, 1992, vol. 13, pp. 277–91.
61. J.Z. Liu: Ph.D. Thesis, Northwestern University, Evanston, IL, 2006.
62. J.Z. Liu, G. Ghosh, A. van de Walle, and M. Asta: *Phys. Rev. B*, 2007, vol. 75, p. 104117.
63. G.W. Lorimer and R.B. Nicholson: *Mechanism of Phase Transformations in Crystalline Solids, Session II*, Institute of Metals, London, 1969, pp. 36–42.
64. K.C. Russell: in *Phase Transformations*, H.I. Aaronson, ed., ASM, Metals Park, OH, 1970, pp. 219–68.
65. R.D. Doherty: in *Physical Metallurgy*, R.W. Cahn and P. Haasen, eds., Elsevier, Amsterdam, 1983, pp. 933–1030.
66. H.I. Aaronson and F.K. LeGoues: *Metall. Trans. A*, 1992, vol. 23A, pp. 1915–45.
67. R. Wagner, R. Kampmann, and P.W. Voorhees: in *Phase Transformations in Materials*, G. Kostorz, ed., Wiley-VCH, New York, NY, 2001, pp. 309–407.
68. B. Chalmers: *Principles of Solidification*, John Wiley & Sons, New York, NY, 1964, pp. 126–28.
69. M.C. Flemings: *Solidification Processing*, McGraw-Hill, New York, NY, 1974, pp. 31–32.
70. W. Kurz and D.J. Fisher: *Fundamentals of Solidification*, 4th ed., Trans Tech Publications, Aedermannsdorf, Switzerland, 1998, p. 15.
71. H.J. Frost and M.F. Ashby: *Deformation-Mechanism Maps: The Plasticity and Creep of Metals and Ceramics*, Pergamon Press, New York, NY, 1982, p. 21.
72. M.A. Meyers and K.K. Chawla: *Mechanical Metallurgy: Principles and Applications*, Prentice-Hall, Englewood Cliffs, NJ, 1984, p. 58.
73. Y. Harada and D.C. Dunand: *Scripta Mater.*, 2003, vol. 48, pp. 219–22.
74. J. Royset and N. Ryum: *Scripta Mater.*, 2005, vol. 52, pp. 1275–79.
75. S. Hori, H. Tai, and Y. Narita: *J. Jpn. Inst. Light Met.*, 1982, vol. 32, pp. 596–603.
76. S. Hori, H. Tai, and Y. Narita: in *Rapidly Quenched Metals*, S. Steeb and H. Warlimont, eds., Elsevier Science Publishers, Wurzburg, 1985, pp. 911–14.
77. K. Asboll and N. Ryum: *J. Inst. Met.*, 1973, vol. 101, pp. 212–14.
78. S.K. Pandey and C. Suryanarayana: *Mater. Sci. Eng. A*, 1989, vol. 111, pp. 181–87.
79. T. Ohashi, K. Suzuki, and R. Ichikawa: *Bull. Nagoya Inst. Technol.*, 1971, vol. 23, pp. 459–65.

80. A. Majumdar, R.H. Mair, and B.C. Muddle: in *Science and Technology of Rapidly Quenched Alloys*, M. Tenhover, W.L. Johnson and L.E. Tanner, eds., MRS, Pittsburgh, PA, 1987, pp. 253–60.
81. J.F. Nie and B.C. Muddle: *Mater. Sci. Eng. A*, 1996, vol. 221, pp. 22–32.
82. N. Ryum: *Acta Metall.*, 1969, vol. 17, pp. 269–78.
83. M. Sundberg, R. Sundberg, and B. Jacobson: *Jernkont. Ann.*, 1971, vol. 155, pp. 1–15.
84. S. Rystad and N. Ryum: *Aluminium*, 1977, vol. 53, pp. 193–95.
85. H. Westengen, L. Auran, and O. Reiso: *Aluminium*, 1981, vol. 57, pp. 797–803.